Transient Experimental and Modelling Studies of Laser-Textured Micro-Grooved Surfaces with a Focus on Piston-Ring Cylinder Liner Contacts

Francisco J. Profito[a,b], Sorin-Cristian Vlădescu[b], Tom Reddyhoff[b], Daniele Dini[b]

[a]Department of Mechanical Engineering, Laboratory of Surface Phenomena (LFS), Polytechnic School of the University of São Paulo, São Paulo, Brazil

[b]Department of Mechanical Engineering, Imperial College London, South Kensington Campus, London, UK

Abstract

This paper presents a comparison between the results from numerical modelling and experiments to shed light on the mechanisms by which surface texture can reduce friction when applied to an automotive cylinder liner. In this configuration, textured features move relative to the piston-liner conjunction and to account for this our approach is to focus on the transient friction response to individual pockets as they pass through, and then leave, the sliding contact. The numerical approach is based on the averaged Reynolds' equation with the Patir & Cheng's flow factors and the p-θ Elrod-Adams mass-conserving cavitation model. The contact pressures that arises from the asperity interactions are solved simultaneously to the fluid flow solution using the Greenwood and Tripp method. The experimental data is produced using a pin-on-disc set up, in which laser textured pockets have been applied to the disc specimen. Under certain conditions in the mixed and boundary lubrication regimes, both model and experimental results show *i*) an increase in friction as the pocket enters the contact, followed by *ii*) a sharp decrease as the pocket leaves the contact, and then *iii*) a gradual decay back to the pre-entrainment value. From the evidence obtained for the first time from the proposed combined modelling and experimental investigation conducted under carefully controlled conditions, we suggest that these three stages occur due to the following mechanisms: *i*) a reduction in fluid pressure due to the increased inlet gap, *ii*) inlet suction as the cavitated fluid within the pocket draws lubricant into the contact, and *iii*) film thickness decay as oil is squeezed out of the contact. The interplay of these three mechanisms is shown to control the response of micro-textured surfaces under all lubrication regimes.

Keywords: Piston Rings, Surface Texture, Numerical Simulations, Mass-conserving Cavitation Model, Mixed Lubrication

1. Introduction

Recent experiments [1, 2, 3] have shown that automotive piston-liner friction may be reduced by up to 50% if the surface of the liner is laser textured with certain configurations of micro-pockets. It is important to model this behaviour to understand and optimise the friction reduction mechanisms that are occurring. However, until now, very few models that predict the lubrication performance of textured surfaces under mixed and boundary lubrication regimes have been successfully compared to experimental data. As shown in very recent literature reviews [4, 5], studies comprising both experimental and theoretical investigations on the effects of laser surface texturing are scarce. The vast majority of these studies focus on hydrodynamic lubrication regime, with just a few of them discussing the impact of textured features under mixed-lubrication regime [6, 7]. This is due to the requirement for them to (i) reproduce experimental configurations with a certain degree of fidelity, (ii) conserve mass

properly, and (iii) account for transient, boundary lubrication conditions. To address this, the current paper presents a comparison between the results from a newly developed numerical model, which fulfils these criteria, and an experimental test rig operating under closely matched conditions.

A general finite volume method (FVM) has recently been proposed for solving Reynolds equation with a mass-conserving cavitation model on irregular grids [8]. This has been applied here to solve textured lubrication problems more effectively than alternative formulations recently proposed in the pertinent literature [9, 10, 11].

A challenge with modelling surface texture is that numerous experiments have shown texture reduces friction in the mixed and boundary regime [12, 13, 14, 15, 16] – but often not in the hydrodynamic regime [17, 18, 19]. However, the majority of texture modelling have included only hydrodynamic behaviour and have largely ignored mixed lubrication and asperity contact. In order to address these issues and provide an effective means of predicting the behaviour of surface texture, we put forward a new modelling approach for textured surface lubrication that is based on the solution of the averaged Reynolds equation using a mass-conserving formulation with the inclusion of flow factors that capture flow through asperities and the contact pressures that arises from the asperity interactions. The focus of this contribution is to specifically look at the behaviour of the fluid and fluid/solid interactions and the local transient effects (cavitation) in the neighbourhood of individual pockets. Both simulation and experimental results obtained from a pin-on-disc test are used to support such investigations.

2. Mathematical Modelling

In this section, the mathematical formulations adopted in this contribution for modelling the mixed lubrication regime of piston-ring cylinder liner contacts are briefly presented. The system configuration showing the main geometric and kinematic features used in the mathematical models is illustrated in Figure 1. The reader is referred to [20] for more details of the modelling and solution framework here discussed.
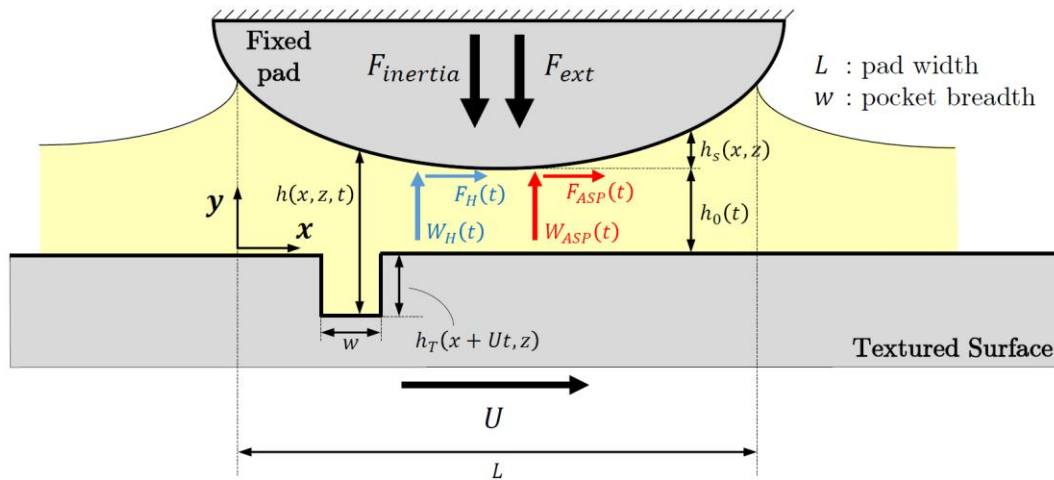

Figure 1 – Schematic illustration of the moving texture contact interface considered in this work. Notice that the fluid flow problem is described with respect to the reference coordinate system attached to the fixed pad (upper surface).

2.1 Fluid Film Lubrication

The hydrodynamic pressure built up over the contact interface under mixed lubrication conditions are mathematically modelled using the average Reynolds equation based on the Patir & Cheng's flow factors formulation [21, 22]. The fluid film cavitation phenomenon is accounted for through the $p - \theta$ Elrod-Adams mass-conserving cavitation model [23, 24], which automatically satisfies the complementary JFO conditions for mass-conservation throughout the lubricated domain [25]. Thus, by assuming the moving texture configuration illustrated in Figure 1 for constant sliding speed, the isothermal average Reynolds equation with $p - \theta$ cavitation model can be expressed as:

$$\frac{\partial}{\partial x}\left[\left(\frac{\phi_{p_x}h^3}{12\mu}\right)\frac{\partial p_H}{\partial x}\right] + \frac{\partial}{\partial z}\left[\left(\frac{\phi_{p_z}h^3}{12\mu}\right)\frac{\partial p_H}{\partial z}\right] = \frac{\partial}{\partial x}\left[\theta\frac{U}{2}\left(h\phi_c + \sigma_R\phi_{s_x}\right)\right] + \frac{\partial(\theta h\phi_c)}{\partial t}$$

(1)

Complementary conditions for cavitation:

$$(p_H - p_{cav})(1 - \theta) = 0 \quad \rightarrow \quad \begin{cases} p_H > p_{cav} & \rightarrow \quad \theta = 1 & (pressured\ regions) \\ p_H = p_{cav} & \rightarrow \quad 0 \leq \theta < 1 & (cavitation\ regions) \end{cases}$$

where $p_H(x, z, t)$ is the hydrodynamic pressure, $h(x, z, t)$ the oil film geometry, U the constant sliding velocity of the moving (bottom) surface, μ the lubricant dynamic viscosity and $\theta(x, z, t)$ the film fraction cavitation parameter [23, 24]. The coefficients ϕ_{p_x} and ϕ_{p_z} are the pressure flow factors, ϕ_{s_x} the shear flow factor along the sliding motion, σ_R is the combined standard deviation of the surface roughness and ϕ_c the contact factor [26, 27]. The lubricant film thickness can be written in the fixed coordinate systems $Oxyz$ as follows (see Figure 1):

$$h(x, z, t) = h_T(x + Ut, z) + h_s(x, z) + h_0(t),$$

(2)

where h_0 is the reference minimum oil film thickness, h_s the fixed pad geometry and h_T the instantaneous geometry of the textured slider moving through the pad.

The solution of Eq. (1) is carried out numerically using a recently proposed hybrid-type finite volume discretization scheme, namely Finite Volume Method based on Elements, for solving Reynolds equation with mass-conserving cavitation model on unstructured meshes [8].

2.2 Asperity Contact Model

The asperity contact pressures that take place due to the surfaces interaction under boundary and mixed lubrication conditions are calculated through the statistical-based Greenwood-Tripp (GT) model for rough contacts [28]:

$$p_{ASP} = \begin{cases} \frac{16\pi\sqrt{2}}{15}E^*\left(\eta_s^2\beta_s^{3/2}\sigma_s^{5/2}\right)F_{5/2}(\bar{h}), & p_{ASP} < H_V \\ H_V, & p_{ASP} \geq H_V \end{cases},$$

(3)

where $p_{ASP}(x, z, t)$ is the asperity contact pressure, $\bar{h}(x, z, t) = \left(\frac{h - Z_s}{\sigma_s}\right)$ the non-dimensional separation distance of the surfaces, E^* the composite elastic modulus, defined as $E^* = \left(\frac{1 - v_1^2}{E_1} + \frac{1 - v_2^2}{E_2}\right)^{-1}$, and H_V the Vickers' hardness of the softer material. The magnitude of the contact pressures relies on the following parameters associated with the statistical distribution of the asperities: Z_s the asperity mean height, σ_s the asperity heights standard deviation, β_s the asperity mean curvature radius and η_s the asperity density. The values of such rough contact parameters are deterministically calculated from 3D surface roughness measurements based on the methodologies described in [29]. In this case, every surface roughness asperity is identified as the local maximum points above the surface reference plane and thus calculations of the asperity mean height, standard deviation, mean curvature radius and density are performed   numerically. The function $F_{5/2}(\bar{h})$, representing the Gaussian distribution of the asperity heights, is approximated by a polynomial function whose coefficients can be found in [20]. Notice that the threshold limit value of H_V imposed to the contact pressures extend the use of elastic GT model to elastic-perfectly plastic contacts. Notice that despite the limitations of the GT model it is still widespread for rough contact calculations and has proven to be robust and efficient to provide satisfactory predictions for surfaces with Gaussian asperity heights distribution as those considered in the present contribution (see Figure 5).

2.3 Equilibrium and Total Friction Equations

The equilibrium equation in y-direction of the system illustrated in Figure 1 can be written as:

$$W_H(t) + W_{ASP}(t) - F_{ext}(t) = m \frac{d^2 h_0}{dt^2}, \tag{4}$$

where $F_{ext}(t)$ is the external force acting on the pad, m the equivalent mass of the vertical moving parts, and $W_H(t)$ and $W_{ASP}(t)$ are the load-carrying forces yielded by the hydrodynamic and asperity contact pressures, which can be expressed considering the integration of the pressures distributions over the pad domain as:

$$\int_{-B/2}^{B/2} \int_{-L/2}^{+L/2} [p_H(x, z, t) + p_{ASP}(x, z, t)] \, dxdz - F_{ext}(t) = m \frac{d^2 h_0}{dt^2}, \tag{5}$$

where L and B are the pad width and the pad length in the z-direction, respectively (see Figure 1).

Similarly, the total friction force on the pad can be calculated by combining the dissipative forces induced by the hydrodynamic and rough contact effects. Accordingly:

$$F(t) = \int\limits_{-B/2}^{B/2} \int\limits_{-L/2}^{+L/2} \left[\underbrace{\left(\frac{h}{2} \frac{\partial p_H}{\partial x} \phi_{fp_x} - \frac{\mu \theta U}{h} \left(\phi_f + \phi_{fs_x} \right) \right)}_{\tau_H(t)} + \underbrace{\left(\mu_{bc} p_{ASP} \right)}_{\tau_{ASP}(t)} \right] dx dz,$$ (6)

where μ_{bc} is the boundary coefficient of friction, $\tau_H(t)$ and $\tau_{ASP}(t)$ the respective hydrodynamic and asperity contact shear stresses, and ϕ_{fs_x} and ϕ_f the shear stress flow factor along the sliding direction and the friction factor defined in the Patir & Cheng's theory [21, 22].

3. Description of the Experimental Tests

All experimental work was carried out using a commercially available Anton Paar high temperature pin-on-disc tribometer (THT), which allowed for friction force measurements on both laser surface textured and smooth, non-textured specimens (see Figure 2).
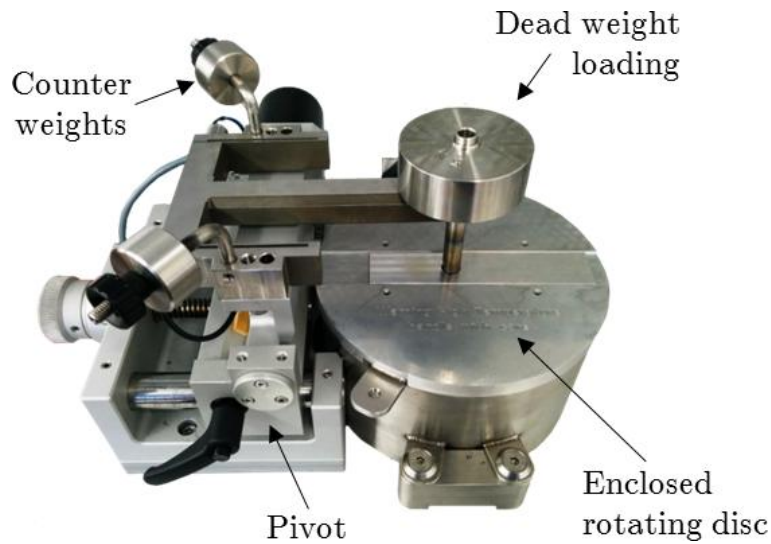
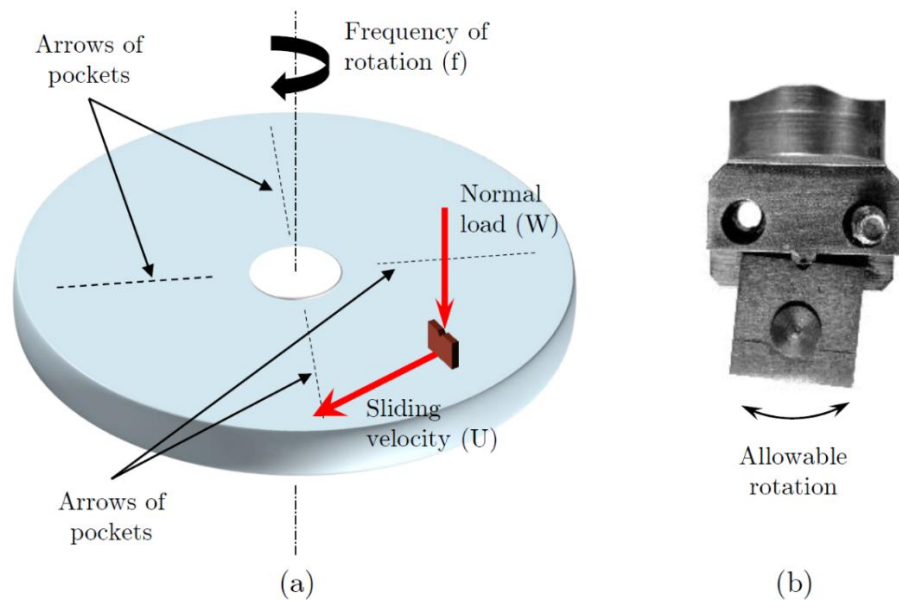Figure 2 – Experimental setup on Anton Paar high temperature tribometer (THT).

Figure 3 – a) Schematic representation of the simulated piston ring/cylinder liner contact for testing at constant sliding speed; b) Front view of the piston ring specimen holder with half of the clamp removed.

The experimental configuration is schematically presented in Figure 3(a); the lower disc specimen simulates the cylinder liner in an IC engine, while the upper specimen was designed to resemble a piston ring. Several adaptations were made to ensure a precise control of test parameters in order to obtain accurate measurements in this "ring-on-disc" configuration. The most noteworthy change was the use of a piston ring specimen holder, depicted in Figure 3(b) with one side of the clamp removed for a visualisation of the small hemisphere that fits into the notch on the upper surface of the piston ring specimen. The holder was designed such that, when the clamp is tightened, the specimen was constrained in the normal and sliding directions, but allowed one rotational degree of freedom so that the bearing could self-align with the disc surface to form a contact with a constant length over time.

The frictional response was determined using the dual LVDT sensors located on each side of the automatic loading arm. This allowed for the minimization of the thermal drift error between measurements, a critical feature when studying the transient influence of a pocket passing through contact. An operating normal load (10 N) was applied by means of dead weights placed on top of the loading arm, while the sliding speed was set to 0.0035 m/s.

In certain cases, it was also necessary to view the distribution of oil and the presence of cavitation within the pocket. To do this, another reciprocating tribometer was used. This alternative setup has been described extensively in previous publications [1, 3, 30] and enables the contact to be viewed from above by a fluorescence microscope that focusses through the transparent reciprocating pad specimen.

3.1. Specimens and Experimental Procedure

The transient effects of textured features sliding through the contact were investigated by employing HPFS Standard Grade fused silica discs that had been laser-textured to produce surface pockets (Oxford Lasers, UK). The pockets' shape and geometrical parameters were selected based on previous

experimental findings by Vladescu and Reddyhoff [1], which showed that textured grooves wider than the contact area in the sliding direction allow for highly pressurised lubricant to leave the contact, resulting in thinner lubricating films. Therefore, to prevent possible pressure-induced flow, an effective surface texture would require features with dimensions smaller than that of the contact zone. For this reason, the textured test specimen was designed to comprise transverse grooves with a minimal width along the sliding direction, and were broken up into segments significantly shorter than the width of the upper piston ring specimen (10 mm).

Figure 4 shows a 2D optical detail of the textured disc, as well as a 3D surface profile of the shape and geometry of the features. The pockets' length, breadth and depth were maintained constant at 1000 µm, 40 µm and 7 µm respectively. The textured disc employed in this study comprised four rows of pockets, displayed along the disc radius at constant circular arcs (see Figure 3a).

The counterpart AISI52100 piston ring specimen was initially hardened to 850 HV and subsequently ground, removing a 0.15 mm stock from all surfaces to achieve a $10 \times 10 \times 2$ mm rectangular pad. On one of the 10×2 mm sides, a self-aligning notch was machined, while the opposite surface was ground to achieve a 20 mm radius. Finally, this convex test surface was mirror-polished to achieve the roughness presented in Figure 5 below.

Three friction tests were performed using the textured and non-textured configurations. Each measurement consisted of a friction vs. time trace showing the transient variations due to the entrainment of 15 pockets (see Figure 14 in Appendix 2). A Matlab® program was written to divide each friction trace into individual pocket entrainments, superimpose them and then make an average. This approach was necessary in order to clearly differentiate the small variation in friction due to the individual pocket from the background noise.
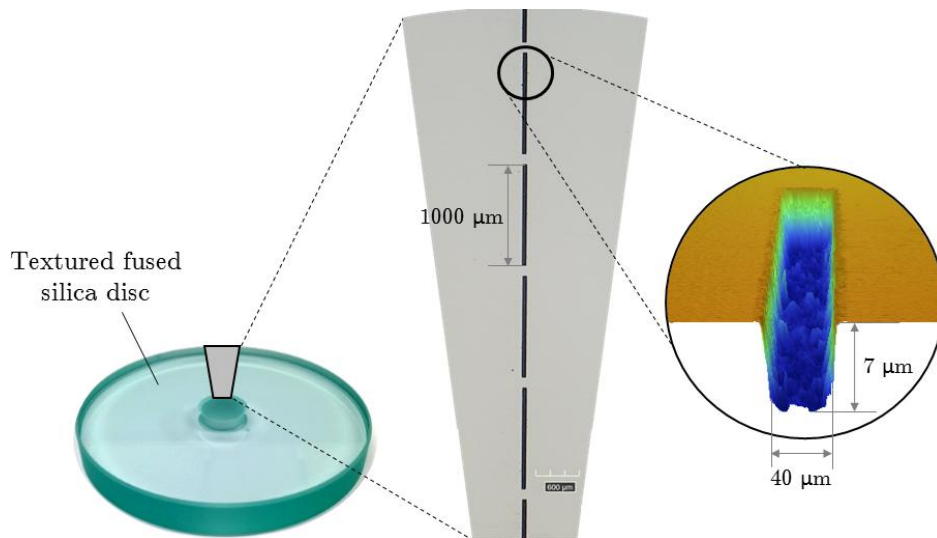
Figure 4 – Two-dimensional surface plot of a section of the laser surface-textured fused silica disc and a 3D surface profile of one pocket.
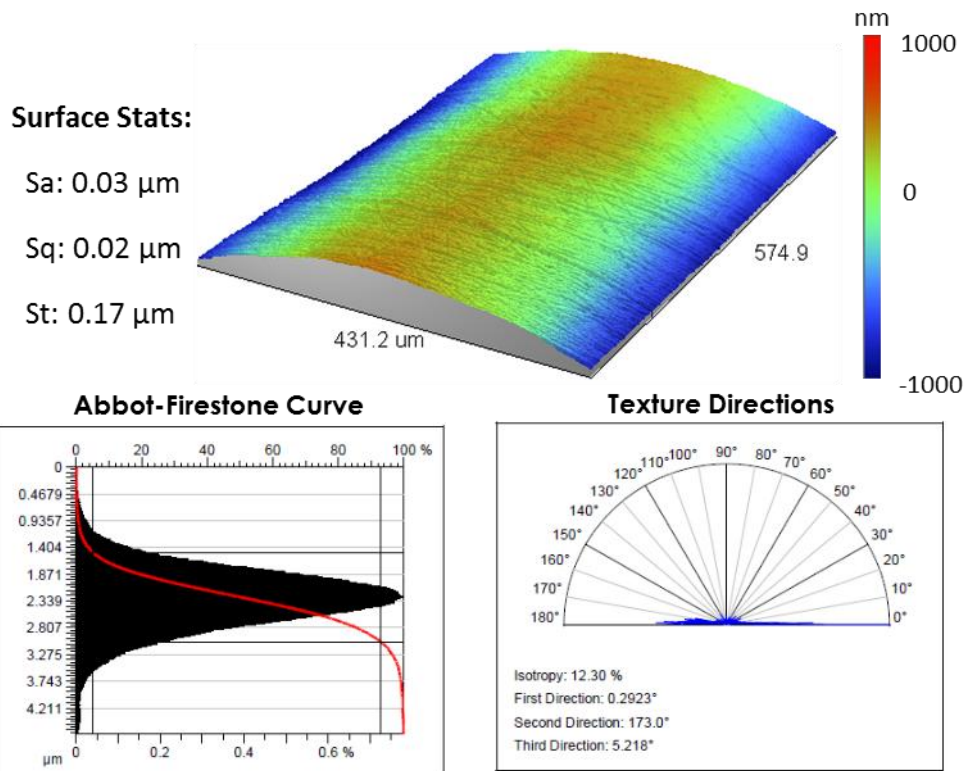
Figure 5 – Three-dimensional surface topography of the barrel-shaped steel specimen as obtained by the Veeco Wyko optical profiler. A surface roughness analysis showed that the roughness heights follow an anisotropic Gaussian distribution.

4. Results and Discussion

4.1. Simulations setup and test case

In order to investigate the cavitation effects at the neighbouring of individual pocket in more detail, the pin-on-disc test described in Section 3 was reproduced through numerical simulation using the mathematical modelling described in Section 2. In this case, time steps of $\Delta t = 0.0025\ s$, $0.00025\ s$ and $0.00025\ s$ were set in the simulations for the sliding speeds of $U = 0.0035$ m/s, 0.035 m/s and 0.35 m/s, respectively, to properly capture details of the transient cavitation effects taking place as the pocket traverses the contact. The chosen values of the time steps were computed using the expression $\Delta t = \Delta x/U$, where Δx is the nodal distance of the grid mesh and U is the sliding speed. Such approach for the temporal discretization was adopted in [31] and ensures that the position of the pocket on the moving surface varies by a nodal distance Δx on the pad grid for each time step Δt, which in turn guarantees the alignment of the film thickness discontinuities and the discretization grid lines; the combined influence of the element size and the increment of the sliding speed was also discussed in [2]. The pad domain where the hydrodynamic and asperity contact problems are solved simultaneously is discretized with a fine mesh containing 10,000 elements (250 x 40 elements, see Figure 6); this mesh provides an optimal solution in terms of accuracy and computational cost for the current configuration. The lubricant and material properties, along with the general test conditions and Greenwood-Tripp asperity parameters of each contact surface are listed in Table 1. The boundary friction coefficient (μ_{BL}) that rules the friction forces under boundary and mixed lubrication conditions was set based on the experimental results of the pin-on-disc test. Furthermore, the values of the flow factors coefficients

needed for calculating the average Reynolds equation (Eq. (1)) and the hydrodynamic friction losses (Eq. (3)) were estimated through the original flow factors curves proposed by Patir & Cheng [21, 22]. Simulation cases for higher speed conditions of 0.035 m/s and 0.35 m/s were also considered in order to evaluate the transient response to individual pocket under mixed and full film lubrication regimes. Such evaluation will also be analysed in accordance with previous experimental reciprocating friction tests reported in [3].
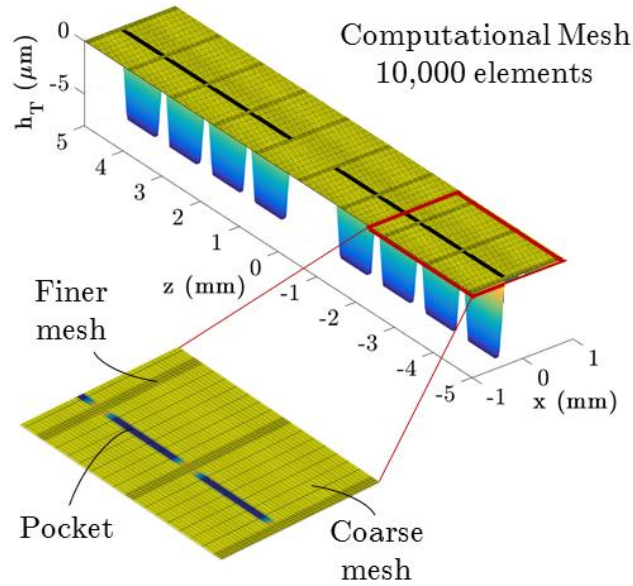
Figure 6 – Film thickness geometry projected on the pad mesh for a given instant as the pocket moves through the pad.

Table 1 – Input parameters for the pin-on-disc test simulations.

Parameter	Values		Unit
	Slider (fused silica)	Pad (AISI 52100 steel)	
E	72.7	210	GPa
υ	0.17	0.30	-
H	1000	850	HV
Sa	0.068	0.088	µm
Sq	0.085	0.102	µm
Z_S	0.11	0.10	µm
σ_S	0.06	0.07	µm
β_S	5.81	4.84	µm
η_S	6.01×10^{10}	4.64×10^{10}	m^{-2}
γ	1	9	-
μ_{BL}	0.12		-
Test Conditions			
Sliding speed	0.0035		m/s
Load	10		N
Lubricant Properties			
Temperature	60		^{o}C
Viscosity	35.09		mPa.s

| Density | 841 | kg/m^3 |

4.2. Experimental vs. Simulation Results

The simulated COF and the variation of the vertical displacement of the pad surface obtained due to the transient effects of the individual moving pocket are depicted in Figure 7 for speeds 0.0035, 0.035 and 0.35 m/s. The film thickness, lubricant pressure, film fraction (cavitation) and asperity contact pressure distributions along the pad centre ($z = 0$) for the (a)-(h) sliding positions illustrated in Figure 7 are shown in Figure 10-Figure 13 (see Appendix). For the lower speed condition (0.0035 m/s), the contact is predicted to be operating mainly in the boundary lubrication regime and the external load is mostly supported by asperity contacts. Here, an abrupt reduction in the friction force is observed as the pocket moves through the concentrated contact region due to the combined local increase in film thickness caused by the pocket depth and the constriction of the effective contact area (see Figure 11d and Figure 12e).

At a higher pocket entrainment velocity (0.035 m/s), the contact is in the mixed lubrication regime so that the load is supported by a combination of asperity contacts and lubricant pressure, both with similar magnitudes. In this case, as highlighted in [3], the transient friction response shows a peak value as the pocket enters the contact (Figure 7). This is associated with the rupture of the lubricant film, since the portion of the contact experiencing hydrodynamic support is reduced (Figure 10b and Figure 11c). This lubricant film rupture is exacerbated by the local cavitation effect produced by the positive normal squeeze (inlet suction) induced by the abrupt increase of the film thickness as the pocket enters the contact, which was not observed for the previous low speed conditions. The images depicted in Figure 8 for two successive positions of the moving pocket over the contact show the lubricant distribution obtained using the fluorescence microscopy set up [3], which reveal the formation of small bubbles at
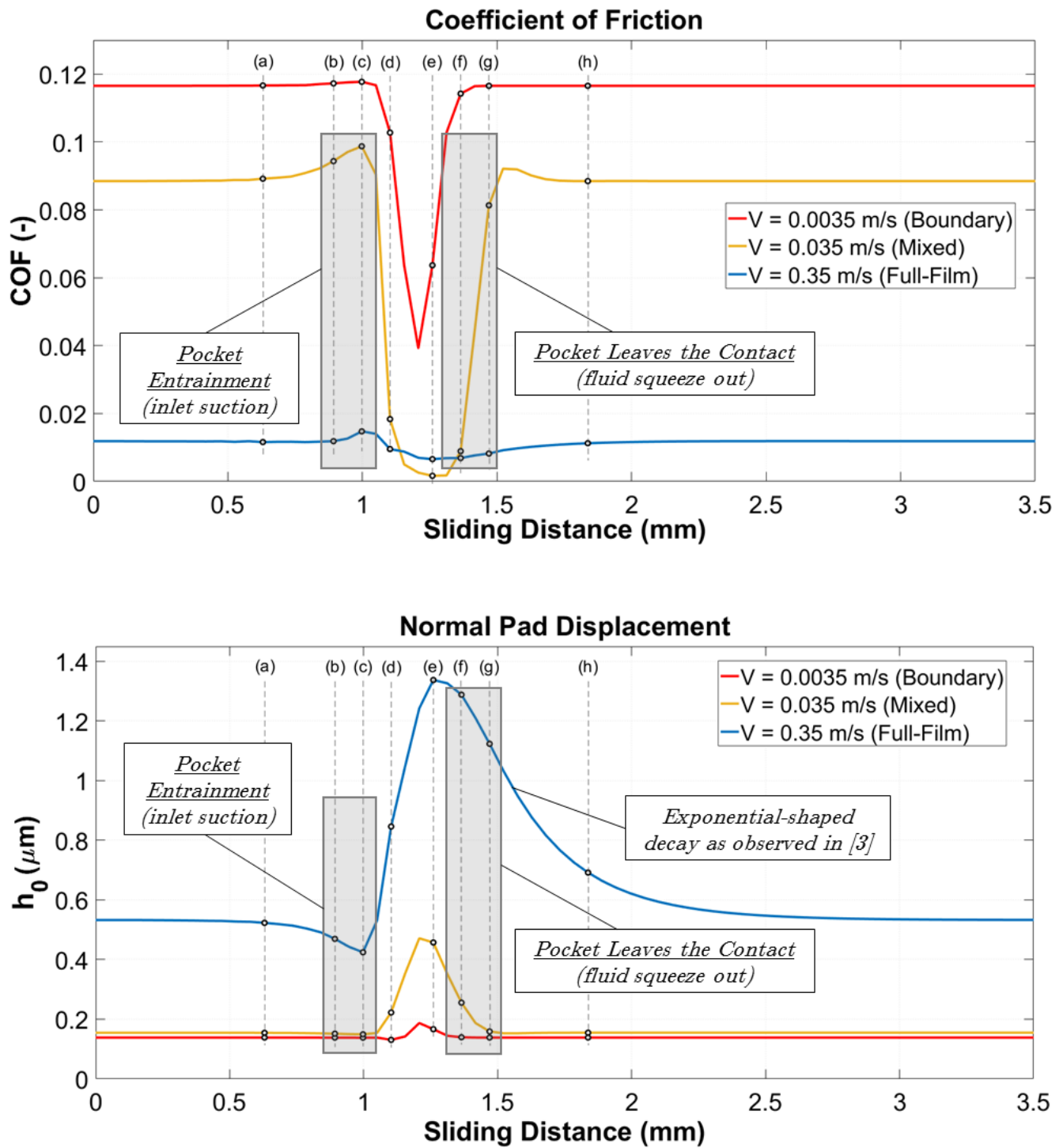
Figure 7 – Variation of the coefficient of friction (top) and normal pad displacement (bottom) over the sliding distance as the moving pocket passes through the fixed pad. Results for three sliding velocities are considered to illustrate the transient effects under different lubrication regimes.
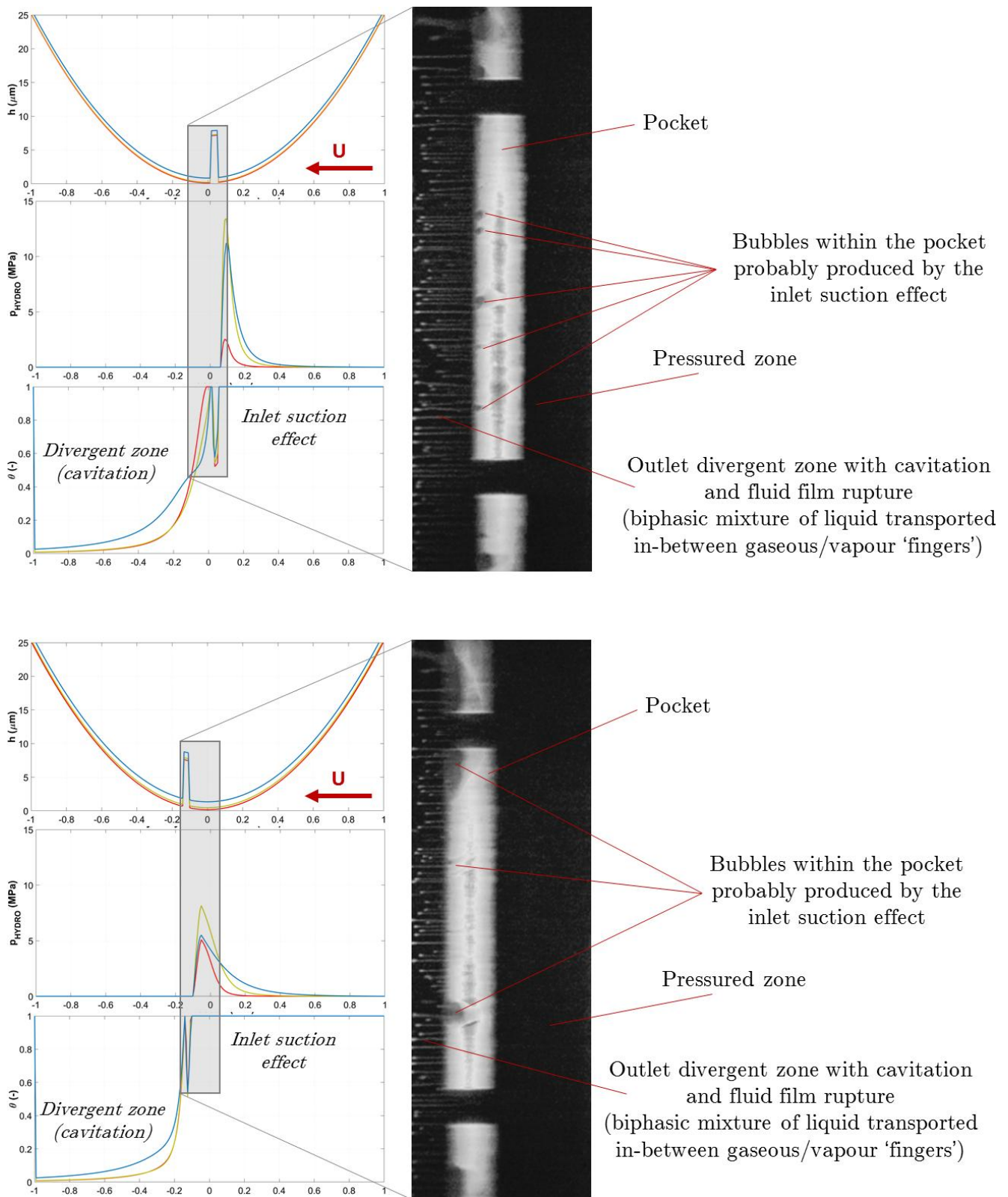
Figure 8 – Predicted hydrodynamic pressure and film fraction (left) and fluorescence images (right) of the moving pocket at the inlet (top) and just after the inlet (bottom) zones measured in the friction tests reported in *[3]*. Both cavitation at the outlet divergent region with fluid film rupture, along with tiny bubbles within the pocket probably associated with the inlet suction effect are shown in the images and correlated with simulated results.
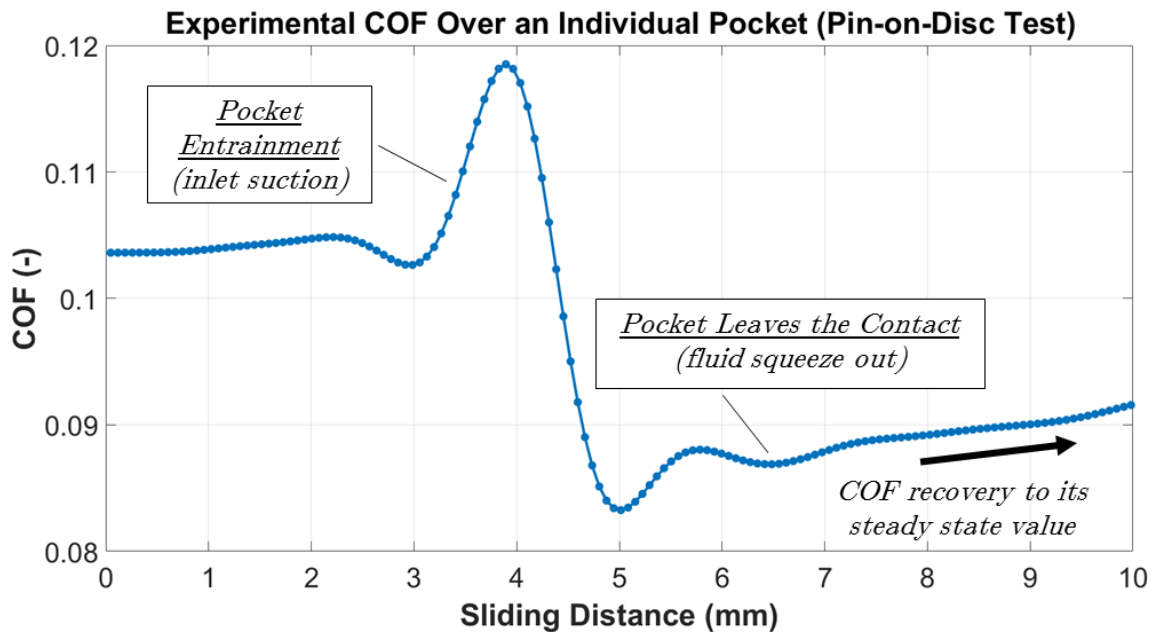
Figure 9 – Average experimental coefficient of friction over an individual pocket measured from the pin-on-disc test described in this work. The experiment was conducted under a (tangential) sliding speed of 0.0035 m/s wherein the contact is predominantly in the mixed lubrication regime.

the leading edge of the pocket as it leaves the contact that might be associated with the inlet suction mechanism. However, the almost instantaneous increase in the friction force is also followed by a steep reduction as the pocket passes through the contact, which we suggest occurs due to inlet suction as described above. What is important is that, due to the boost in pressure caused by inlet suction, the film thickness when the pocket leaves the contact is greater than before the pocket enters – *i.e.* the overall effect of the pocket under these conditions is a net increase in film thickness. This leads to the exponential-shaped decay of the pad's vertical displacement after the pocket leaves the concentrated contact region and the lubricant is squeezed out from between the surfaces; this is also in agreement with film thickness measurements reported in [3]. Although not modelled here, it can be envisioned that if a subsequent pocket entrainment occurs before the film thickness has decayed down to its steady state value the film thickness may be boosted further. As previously shown experimentally in [3], if the period between pockets being entrained into the contact is less than the squeeze film decay time, a consistently lower friction (compared to a non-textured liner component) will be achieved.

In the full-film regime with inlet velocity of 0.35 m/s, in which the external load is completely supported by the fluid pressure, the peak in friction force observed in the mixed case is also present at the entrainment zone due to the same film reduction effect (Figure 7). Under this lubrication condition, however, the magnitudes of friction are obviously lower and the abrupt decrease in the COF is not observed since no asperity interaction takes place (*i.e.* for thicker films, shape of the Stribeck curve means friction is insensitive to increase in film thickness). In fact, a slight reduction in the friction force can be seen just after the pocket enters the contact, but with no substantial influence on the overall COF. This lack of significant benefit of textures under full hydrodynamic conditions has also been detected experimentally in [3]. Thus, while in boundary and mixed lubrication regimes the advantages of textures are obvious, in full-film situations this might not always be the case. A further consideration regarding the small overall reduction in COF obtained through this simulation is that as the COF first

increases (inlet zone) and then decreases; therefore, the variation in COF may be largely dependent on the dynamics and speed of response of the test rig, pockets size/depth and other details that are not yet contemplated in the analysis, and both an overall increase or decrease of friction coefficient might be experienced in such circumstances as already shown experimentally in [3].

The seeming impact of the inlet suction mechanism on the COF is supported by the simulation results for the mixed and full-film regimes, which are summarized in Figure 10-Figure 13 (see Appendix 1). Furthermore, this behaviour appears to be supported by experimental observations made during friction testing of texture specimens. As can be seen in Figure 7 the experiment conducted predominantly under mixed conditions gave results that were qualitatively in agreement with the simulation (Figure 7) for the same regime. Here, it is evident that there is an initial increase and then a decrease in COF as the pocket travels through the contact zone.

Although the qualitative agreement between numerical and experimental COF signals is encouraging, there is some discrepancy between them, which should be discussed. Specifically, for the pin-on-disc test conditions here considered (U = 0.0035 m/s), the model predicts predominantly boundary lubrication (Figure 7) whereas the experimental results indicate mixed regime (Figure 9). This issue is probably related to the fact that the system seems to be operating at the border between boundary and mixed regimes, in which small changes in the simulation inputs (especially the flow factors and the statistical asperity contact parameters) are very sensitive and prone to make the models predict boundary rather than mixed regime. Furthermore, this might also be linked to the intrinsic difficulty in modelling effectively and the local inlet suction cavitation phenomenon and the oscillatory squeeze motion that governs the transient response of the system, along with the limitations of the rough contact model adopted to deal with anisotropic surfaces (see Figure 5) and large proportions of real contact area. Particularly regarding the rough contact modelling, the coupling of more advanced methodologies including the use of deterministic models of interactions between rough surfaces, similar to those already developed by some of the authors [32, 33, 34], with the fluid flow solution at the roughness scale could be contemplated to deal with anisotropic non-Gaussian surfaces under severe contact conditions. This indeed provides new challenges to perform even more accurate mathematical modelling and improved experimental configurations to provide a more in depth understanding of the effects of local, transient cavitation mechanisms occurring at the neighbourhood of textures on the overall system tribological performance. These initial simulation results, appear however to have captured for the first time the main features of the transient experimental signals and thus provide an important step forward.

5. Conclusions

In this study, we have performed simulations of the transient response of a piston-ring cylinder liner contact to the entrainment of individual surface texture features, under different lubrication regimes. For the first time comparisons were made with well controlled experiments, performed using a new "ring-on-disc" configuration and test results recently reported in the literature (obtained by some of the authors of the present contribution using a reciprocating rig), and these have been presented and discussed to shed light on the mechanisms governing the frictional response of this assembly under different lubrication regimes. We have placed particular emphasis on the mechanisms responsible for the benefit that laser-textured micro-grooved surfaces provide in terms of reduced COF under boundary and mixed lubrication, emphasising the interplay between different phenomena that affect the

instantaneous and overall lubrication response of the contact pair. It was shown that inlet suction, asperity contacts and fluid squeeze out all contribute to the response of system and their relative contribution may differ depending on the operating regime. The agreement between experimental and modelling results, both in terms of transient friction response and formation of cavitation within the pockets, is very encouraging and shows that the proposed method is capable of capturing the key features that govern micro-textured contacts. Finally, it was also shown that the micro-grooved samples employed in this study have little effect on the overall frictional response in the hydrodynamic regime and that, again, the response of the system in this regime is also affected by various parameters and running conditions. Particularly, it is worth highlighting that while these results are conclusive in the context of the present contribution, more general investigations considering the presence of multiple textures and their shape and topological distribution within the contact, together with the attempt to achieve full quantitative agreement between experiments and simulations, are required to provide more general trends. This is being currently studied and will be the subject of future contributions.

Appendix 1 – Snapshots of transient simulation results

Snapshots of the transient simulations are shown in Figure 10 - Figure 13. Each of the plots shows the film thickness, fluid pressure, film fraction (cavitation) and asperity contact pressure along the pad center (z = 0) for the (a)-(h) sliding positions illustrated in Figure 7. These figures can be used to have an overall idea on the variation of the fluid and asperity contact pressures and cavitation zones before, during and after the pocket entrainment.
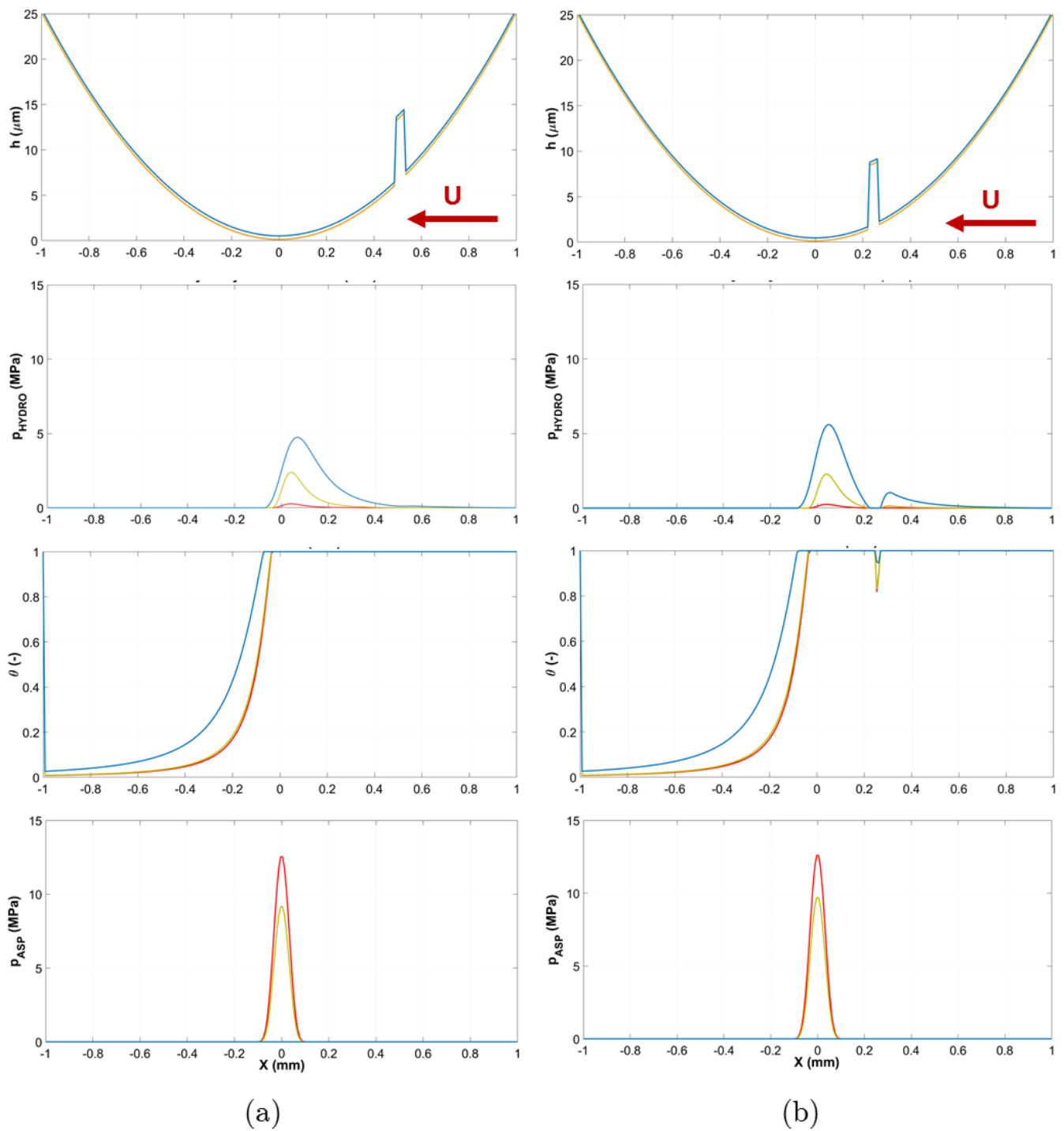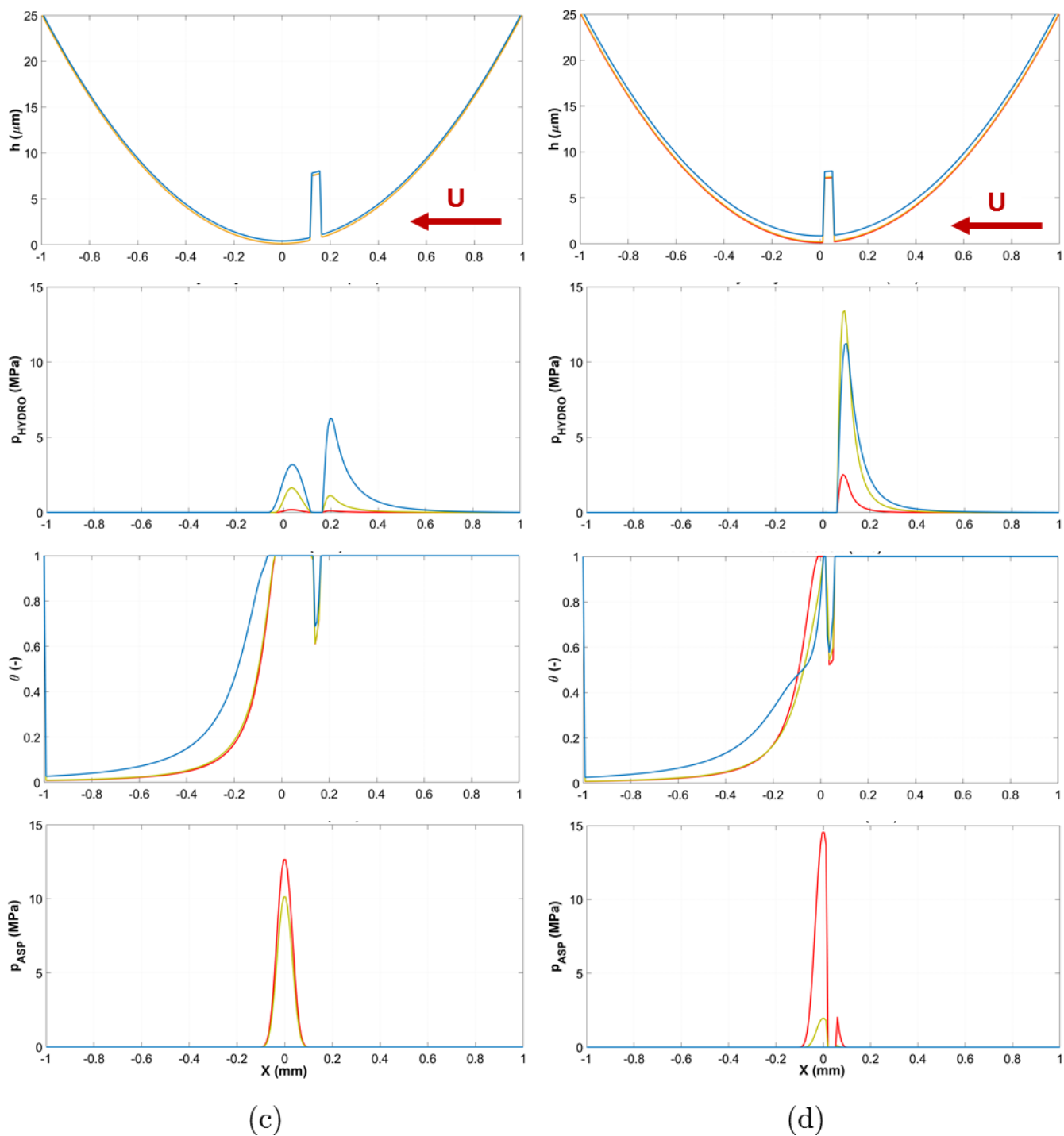
Figure 10 – Variation of the film thickness, fluid pressure, film fraction (cavitation) and asperity contact pressure along the pad center *(z = 0)* over the sliding distance **before** the pocket entrainment. (a) and (b) are the sliding positions compatible with those illustrated in Figure 7. V = 0.0035 m/s (red, boundary regime), V = 0.035 m/s (yellow, mixed regime) and V = 0.35 m/s (blue, full-film regime).
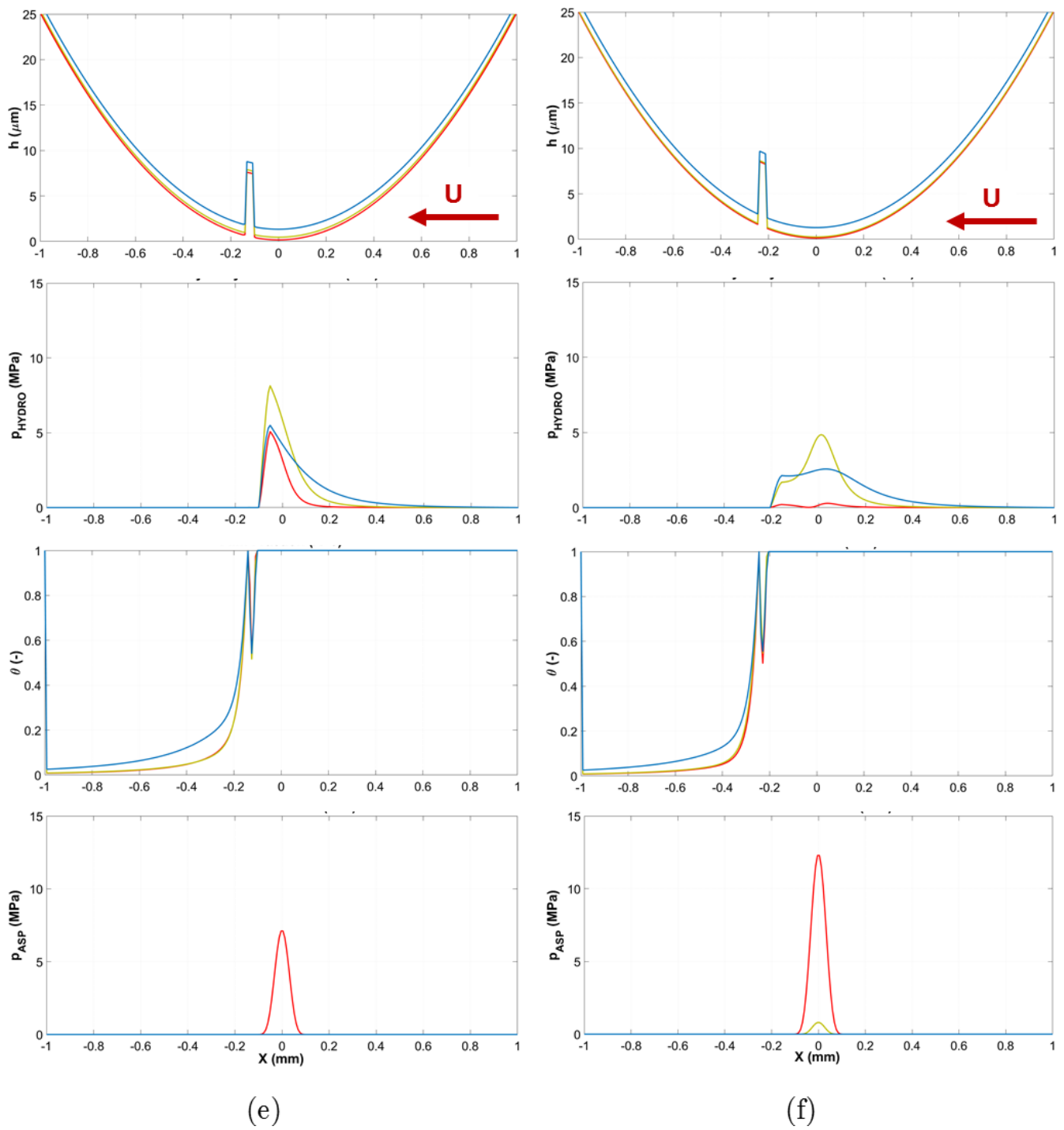
Figure 11 – Variation of the film thickness, fluid pressure, film fraction (cavitation) and asperity contact pressure along the pad center ($z = 0$) over the sliding distance **<u>during</u>** the pocket entrainment. (c) and (d) are the sliding positions compatible with those illustrated in Figure 7. V = 0.0035 m/s (red, boundary regime), V = 0.035 m/s (yellow, mixed regime) and V = 0.35 m/s (blue, full-film regime).
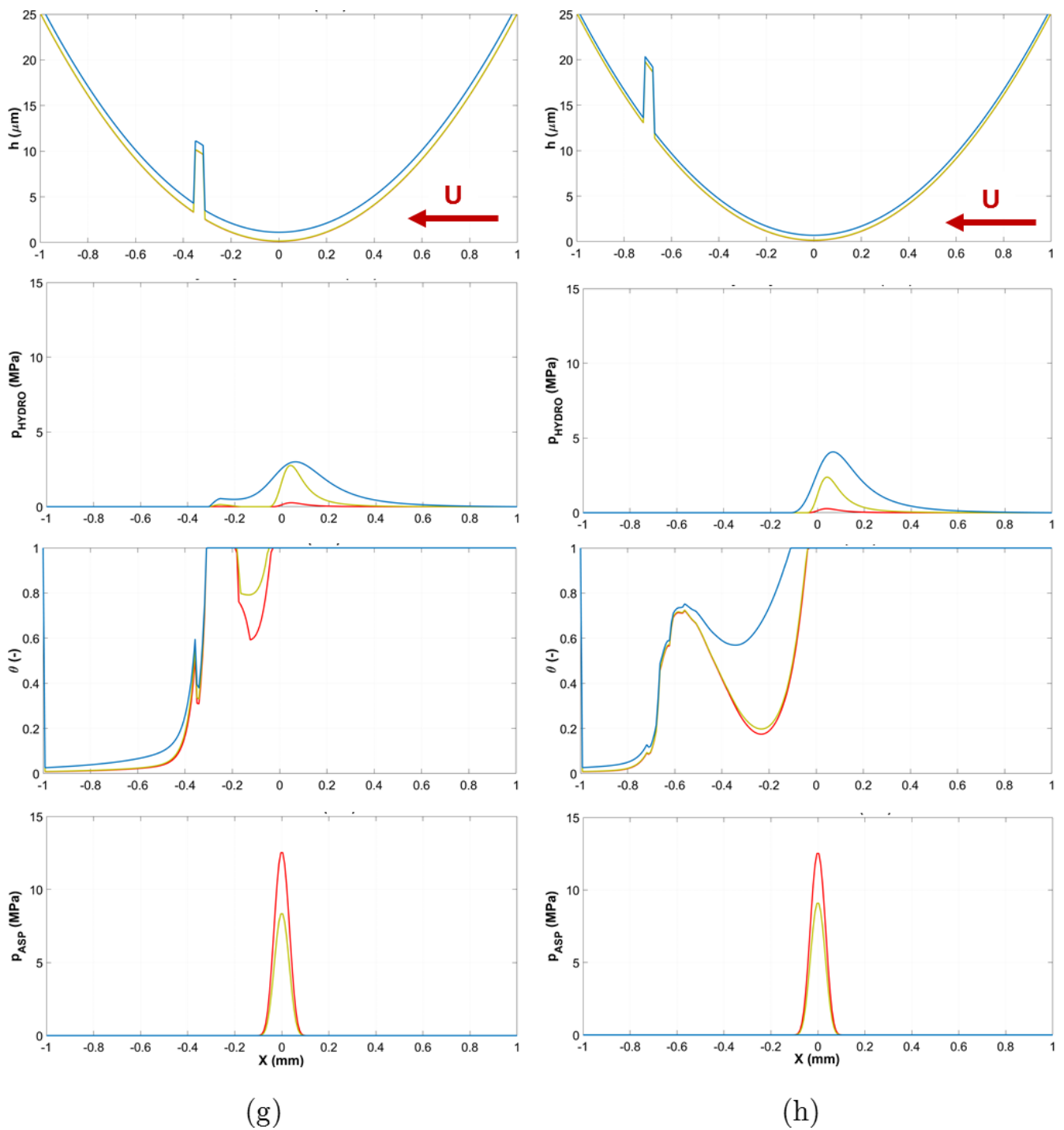
Figure 12 – Variation of the film thickness, fluid pressure, film fraction (cavitation) and asperity contact pressure along the pad center ($z = 0$) over the sliding distance **as the pocket leaves the contact**. (e) and (f) are the sliding positions compatible with those illustrated in Figure 7. V = 0.0035 m/s (red, boundary regime), V = 0.035 m/s (yellow, mixed regime) and V = 0.35 m/s (blue, full-film regime).

Figure 13 – Variation of the film thickness, fluid pressure, film fraction (cavitation) and asperity contact pressure along the pad center (z = 0) over the sliding distance **after the pocket leaves the contact**. (g) and (h) are the sliding positions compatible with those illustrated in Figure 7. V = 0.0035 m/s (red, boundary regime), V = 0.035 m/s (yellow, mixed regime) and V = 0.35 m/s (blue, full-film regime).

Appendix 2 – Averaging of experimental results

Figure 14 shows the raw friction versus sliding distance trace before any averaging technique has been applied. The increase and subsequent decrease in friction that occurs as each pocket passes through the contact is clearly visible. However, it can also be seen that there is a significant amount of background noise due to roughness variations and the waviness of the specimen surface. For this reason, a Matlab® program was written to divide the friction trace into sections, each containing a set number of pocket entrainments (as shown by dashed vertical lines in Figure 14 for single pocket entrainments). The program then obtained the average variation in friction by superimposing these sections onto a single distance axis (ensuring that the maximum friction value for each pocket entrainment occurred at the same location). Figure 15 shows such an averaged trace in which three subsequent entrainments have been captured, whilst Figure 9 focuses on the zoomed-in view of just one pocket entrainment.
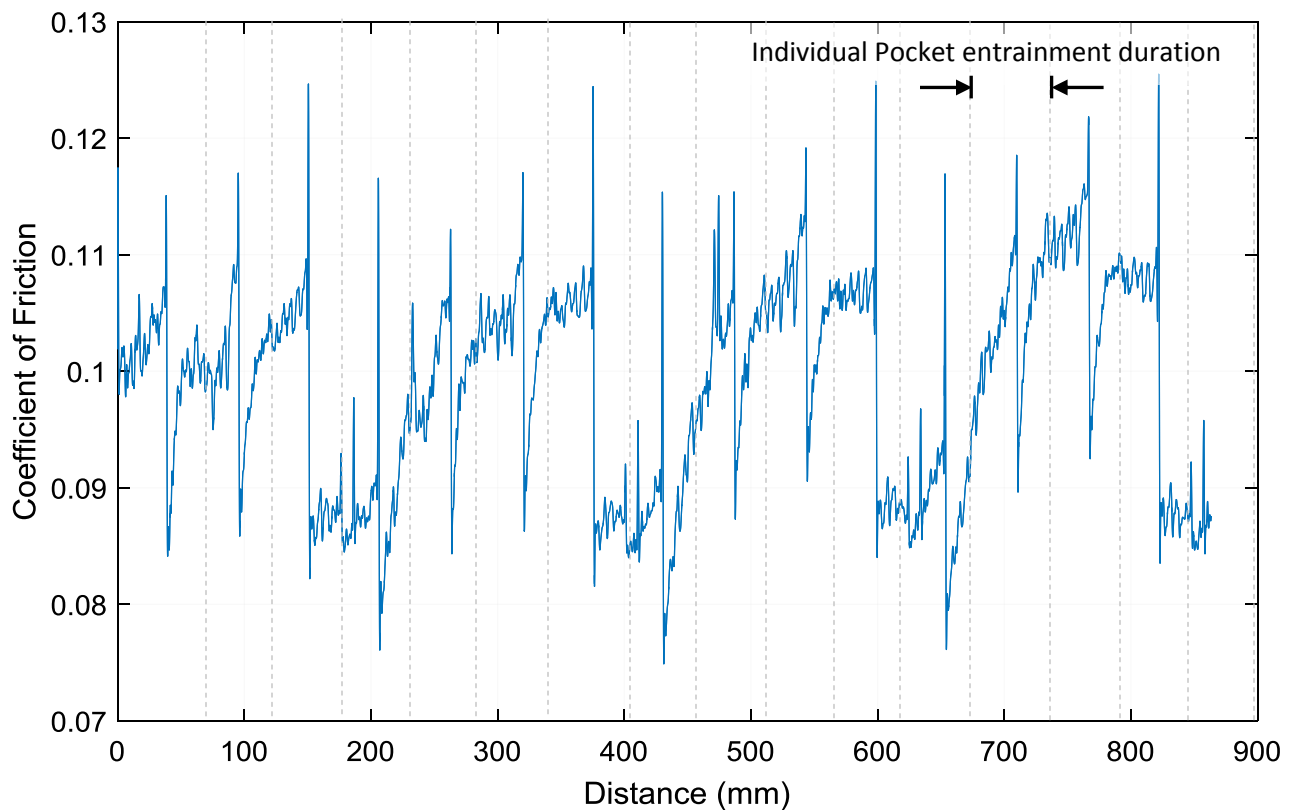

Figure 14 – Raw experimental coefficient of friction data, obtained using the pin-on-disc setup from a test in which 15 pocket entrainments were observed. The experiment was conducted under a (tangential) sliding speed of 0.0035 m/s wherein the contact is predominantly in the mixed lubrication regime.
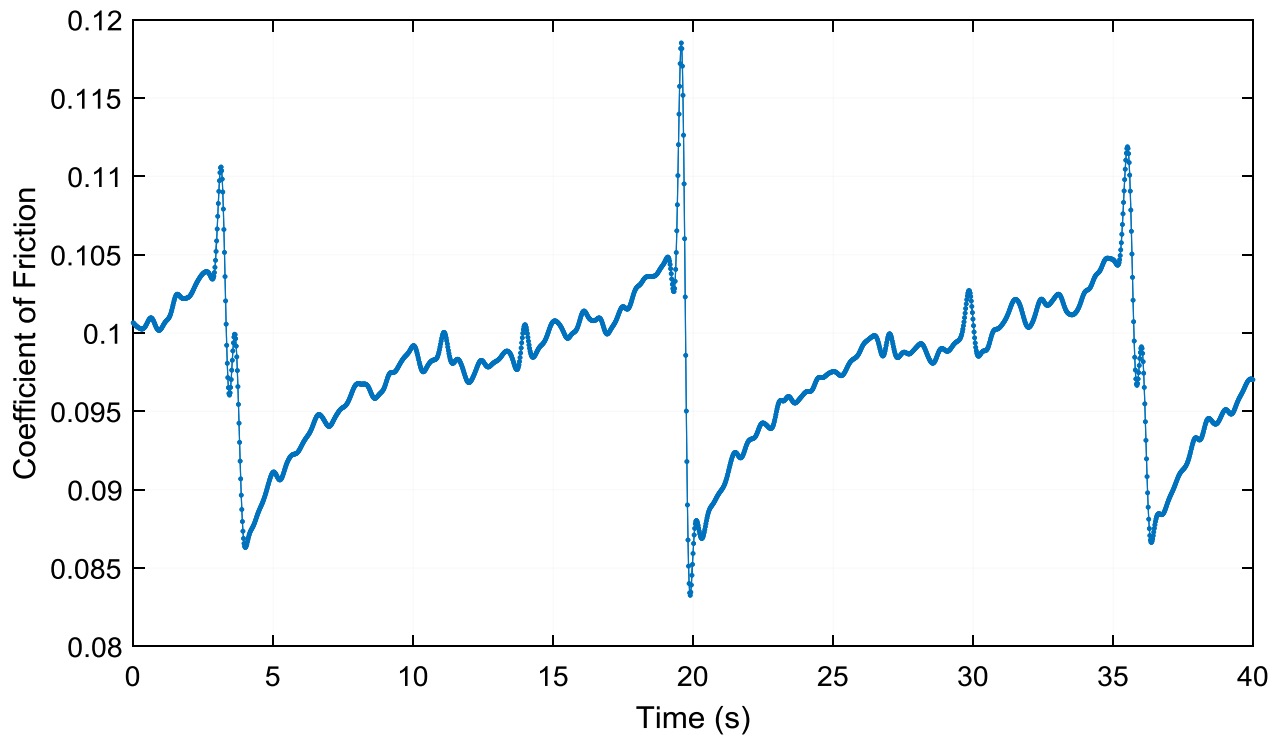
Figure 15 – Averaged experimental coefficient of friction, showing 3 pocket entrainments. The experiment was conducted under a (tangential) sliding speed of 0.0035 m/s wherein the contact is predominantly in the mixed lubrication regime.

References

[1]   S.-C. Vlădescu, A. Olver, I. Pegg e T. Reddyhoff, "The effects of surface texture in reciprocating contacts – An experimental study," *Tribology International,* vol. 82, pp. 28-42, 2015.

[2]   S. Medina, M. Fowell, S.-C. Vlădescu, T. Reddyhoff, I. Pegg, A. Olver e D. Dini, "Transient effects in lubricated textured bearings," *Proceedings of the Institution of Mechanical Engineers, Part J: Journal of Engineering Tribology,* vol. 229, nº 4, pp. 523-537, 2015.

[3]   S.-C. Vlădescu, S. Medina, A. Olver, I. Pegg e T. Reddyhoff, "The transient friction response of a laser textured, reciprocating contact to the entrainment of individual pockets," *Tribology Letters,* vol. (Forthcoming), 2016.

[4]   D. Gropper, L. Wang e T. J. Harvey, "Hydrodynamic lubrication of textured surfaces: A review of modeling techniques and key findings," *Tribology International,* vol. 94, pp. 509-529, 2016.

[5]   U. Sudeep, N. Tandon e R. Pandey, "Performance of Lubricated Rolling/Sliding Concentrated Contacts With Surface Textures: A Review," *Journal of Tribology,* vol. 137, p. 031501, 2015.

[6]   L. Mourier, D. Mazuyer, A. Lubrecht and C. Donnet, "Transient increase of film thickness in micro-textured EHL contacts," *Tribology International,* vol. 39, p. 1745–1756, 2006.

[7]   A. Ramesh, W. Akram, S. Mishra, A. Cannon, A. Polycarpou e W. King, "Friction characteristics of microtextured surfaces under mixed and hydrodynamic lubrication," *Tribology International,* vol. 57, p. 170–176, 2013.

[8]   F. Profito, M. Giacopini, D. Zachariadis and D. Dini, "A general finite volume method for the solution of the Reynolds lubrication equation with a mass-conserving cavitation model," *Tribology Letters,* vol. 60, no. 1, 2015.

[9]   M. Giacopini, M. Fowell, D. Dini e A. Strozzi, "A mass-conserving complementary formulation to study lubricant films in the presence of cavitation," *Journal of Tribology,* vol. 132, nº 4, p. 041702, 2010.

[10] L. Bertocchi, D. Dini, M. Giacopini, M. Fowell e A. Baldini, "Fluid film lubrication in the presence of cavitation: a mass-conserving two-dimensional formulation for compressible, piezoviscous and non-Newtonian fluids," *Tribology International,* vol. 67, pp. 61-71, 2013.

[11] T. Woloszynski, P. Podsiadlo e G. Stachowiak, "Efficient Solution to the Cavitation Problem in Hydrodynamic Lubrication," *Tribology Letters,* vol. 58, nº 18, pp. 1-11, 2015.

[12] U. Pettersson e S. Jacobson, "Influence of surface texture on boundary lubricated sliding contacts," *Tribology International,* vol. 36, pp. 857-864., 2003.

[13] U. Pettersson e S. Jacobson, "Friction and Wear Properties of Micro Textured DLC Coated Surfaces in Boundary Lubricated Sliding," *Tribology Letter,* vol. 17, pp. 553-559., 2004.

[14] D. Braun, C. Greiner, S. J. e P. Gumbsch, "Efficiency of laser surface texturing in the reduction of friction under mixed lubrication," *Tribology International,* vol. 77, pp. 142-147., 2014.

[15] W. Wang, Z. Huang, D. Shen, L. Kong e S. Li, "The Effect of Triangle-Shaped Surface Textures on the Performance of the Lubricated Point-Contacts," *Journal of Tribology,* vol. 135, p. 021503, 2013.

[16] X. K. M. Lu, "An Experimental Investigation of Dimple Effect on the Stribeck Curve of Journal Bearings," *Tribology Letters,* vol. 27, pp. 169-176., 2007.

[17] A. Kovalchenko, O. Ajayi, A. Erdemir, G. Fenske e I. Etsion, "The Effect of Laser Surface Texturing on Transitions in Lubrication Regimes During Unidirectional Sliding Contact," *Tribology International,* vol. 38, pp. 219-225., 2005.

[18] A. Borghi, E. Gualtieri, M. D. L. Moretti e S. Valeri, "Tribological effects of surface texturing on nitriding steel for high-performance engine applications," *Wear,* vol. 265, pp. 1046-1051., 2008.

[19] S.-C. Vlădescu, A. Olver, I. Pegg e T. Reddyhoff, "Combined friction and wear reduction in a reciprocating contact through laser surface texturing," *Wear,* Vols. %1 de %2358-359, pp. 51-61, 2016.

[20] F. Profito, S.-C. Vlădescu, T. Reddyhoff e D. Dini, "Experimental Validation of a Mixed-Lubrication Regime Model for Textured Piston-Ring-Liner Contacts," *ASTM International Journal on Materials Performance and Characterization - Special Issue on Surface Texturing for Improved Tribological Performance,* p. In Press, 2016.

[21] N. Patir and H. S. Cheng, "An average ow model for determining effects of three-dimensional roughness on partial hydrodynamic lubrication," *Journal of Lubrication Technology,* vol. 100, no. 1, pp. 12-17, 1978.

[22] N. Patir and H. S. Cheng, "Application of average flow model to lubrication between rough sliding surfaces," *Journal of Lubrication Technology,* vol. 101, no. 2, pp. 220-229, 1979.

[23] H. Elrod e M. L. Adams, "A computer program for cavitation and starvation problems," em *In Cavitation and related phenomena in lubrication: proceedings of the 1st Leeds-Lyon Symposium on Tribology, held in the Institute of Tribology, held in the Institute of Tribology, Department of Mechanical Engineering, University of Leeds, September 1974*, Leeds, England, 1974.

[24] H. G. Elrod, "A cavitation and starvation algorithm," *Journal of Lubrication Technology,* vol. 103, no. 3, pp. 350-354, 1981.

[25] L. Floberg, "Cavitation boundary conditions with regard to the number of streamers and tensile strength of the liquid," in *In Cavitation and related phenomena in lubrication: proceedings of the 1st Leeds-Lyon Symposium on Tribology, held in the Institute of Tribology, Department of Mechanical Engineering, University of Leeds, England, September 1974*, 1974.

[26] F. Meng, Q. Wang, D. Hua and S. Liu, "A simple method to calculate contact factor used in average ow model," *Journal of Tribology,* vol. 132, no. 2, p. 024505, 2010.

[27] P. Wang, T. Keith Jr. and K. Vaidyanathan, "Combined surface roughness pattern and non-Newtonian effects on the performance of dynamically loaded journal bearings," *Tribology Transactions,* vol. 45, no. 1, pp. 1-10, 2002.

[28] J. Greenwood e J. H. Tripp, "The contact of two nominally at rough surfaces," *Proceedings of the Institution of Mechanical Engineers,* vol. 185, nº 1, pp. 625-633, 1970.

[29] E. Tomanik, "Modelling of the asperity contact area on actual 3D surfaces," *SAE Technical Paper,* pp. 2005-01-1864, 2005.

[30] S.-C. Vlădescu, S. Medina, A. Olver, I. Pegg e T. Reddyhoff, "Lubricant film thickness and friction force measurements in a laser surface textured reciprocating line contact simulating the

piston ring – Liner pairing," *Tribology International,* vol. (Forthcoming), 2016.

[31] A. Gherca, A. Fatu, M. Hajjam e P. Maspeyrot, "Effects of surface texturing in steady-state and transient flow conditions: Two-dimensional numerical solution using a mass-conserving cavitation model," *Proc IMechE Part J: Journal of Engineering Tribology,* vol. 229, nº 4, pp. 505-522, 2015.

[32] S. Medina e D. Dini, "A numerical model for the deterministic analysis of adhesive rough contacts down to the nano-scale," *International Journal of Solids and Structures,* vol. 51, pp. 2620-2632, 2014.

[33] S. Medina, D. Nowell e D. Dini, "Analytical and Numerical Models for Tangential Stiffness of Rough Elastic Contacts," *Tribology Letters,* vol. 49, pp. 103-115, 2013.

[34] S. Medina, A. Olver e D. Dini, "The Influence of Surface Topography on Energy Dissipation and Compliance in Tangentially Loaded Elastic Contacts," *Journal of Tribology,* vol. 134, pp. 011401-1, 2012.